

Computational and Experimental Study of the Structure, Binding Preferences, and Spectroscopy of Nickel(II) and Vanadyl Porphyrins in Petroleum

Stanislav R. Stoyanov,[†] Cindy-Xing Yin,[‡] Murray R. Gray,[‡] Jeffrey M. Stryker,[§] Sergey Gusarov,[†] and Andriy Kovalenko^{*,†,||}

National Institute for Nanotechnology, National Research Council of Canada, 11421 Saskatchewan Drive, Edmonton, AB, T6G 2M9, Canada; Department of Chemical and Materials Engineering, University of Alberta, Edmonton, Alberta, Canada; Department of Chemistry, University of Alberta, Edmonton, Alberta, Canada; and Department of Mechanical Engineering, University of Alberta, Edmonton, Alberta, Canada

Received: September 9, 2009; Revised Manuscript Received: December 7, 2009

We present a computational exploration of five- and six-coordinate Ni(II) and vanadyl porphyrins, including prediction of UV–vis spectroscopic behavior and metalloporphyrin structure as well as determination of a binding energy threshold between strongly bound complexes that have been isolated as single crystals and weakly bound ones that we detect by visible absorption spectroscopy. The excited states are calculated using the tandem of the time-dependent density functional theory (TD-DFT) and the conductor-like polarizable continuum model (CPCM). The excited-state energies in chloroform solvent obtained by using two density functionals are found to correlate linearly with the experimental Soret and α -band energies for a known series of five-coordinate vanadyl porphyrins. The established linear correction allows simulation of the excited states for labile octahedral vanadyl porphyrins that have not been isolated and yields Soret and α -band bathochromic shifts that are in agreement with our UV–vis spectroscopic results. The PBE0 and PW91 functionals in combination with DNP basis set perform best for both structure and binding energy prediction. The reactivity preferences of Ni(II) and vanadyl porphyrins toward aromatic fragments of large petroleum molecules are explored by using the density functional theory (DFT). Analysis of electrostatic potentials and Fukui functions matching shows that axial coordination and hydrogen bonding are the preferred aggregation modes between vanadyl porphyrins and nitrogen-containing heterocycle fragments. This investigation improves our understanding on the cause for broadening of the Ni and V porphyrin Soret band in heavy oils. Our findings can be useful for the development of metals removal methods for heavy oil upgrading.

Introduction

First-row transition metals, such as V and Ni, are present in bitumen at concentrations up to 1320 ppm, depending upon the source.^{1,2} Nickel(II) and vanadyl porphyrins found in crude oils and bitumens are thought to be derived from Mg(II) porphyrins in chlorophylls during diagenesis. Magnesium(II) porphyrin derivatives are easily demetalated and the metal ion is replaced by V or Ni because these form inert porphyrin complexes. Despite the low natural abundance of V and Ni in the earth's crust, vanadyl and Ni(II) porphyrins are highly robust and persist over geological time periods.³ The Ni(II) and vanadyl porphyrin complexes⁴ are easily observed due to their specific absorption spectroscopic characteristics.⁵ The visible spectrum Soret band absorbance of Ni and V porphyrins, however, accounts for only 40% of the total metals present in asphaltenes, based on extinction coefficients obtained from isolated compounds.⁶ In the model of petroleum asphaltene macrostructure of Dickie et al., it has been proposed that petroporphyrins stack with the aromatic sheets of polycyclic asphaltene compounds.⁷ Our recent findings do not support this model because π – π interaction between large alkylaromatics or bridged aromatics and model vanadyl or Ni(II) porphyrins has not been detected. We have

proposed that petroporphyrins that do not contribute a strong Soret band in UV–vis spectroscopy are covalently attached to larger aromatics and bound to other asphaltene molecules.⁸ The relevance of such elaborated porphyrin compounds has recently been supported by studies showing the presence of vanadyl porphyrins that contain additional fused phenyl and thiophene rings, although the exact structures of these complexes are not known.⁹ The V and Ni in petroporphyrins are important contaminants in bitumens and heavy oils. A better understanding of their chemical structure and spectroscopic behavior is the key to developing improved processing technology.

Nickel(II) and vanadyl porphyrins have rather low reactivity toward axial coordination. In Ni(II) porphyrins, this is due to the d^8 electron configuration that precludes a preference toward square-planar coordination. However, in the presence of excess ligand, such as pyridine, the orbital overlapping and mixing between the ligand lone pair orbitals and the Ni d_{z^2} orbital provide energetically favorable conditions for one of the $3d_{z^2}$ electrons to be promoted to the $3d_{x^2-y^2}$ orbital, as the degree of interaction with the basic nitrogen of the ligand increases. This mechanism, first recognized by Caughey et al., explains the triplet ground state of six-coordinate Ni(II) porphyrins.¹⁰ Holten and co-workers have performed extensive photophysical studies on four-coordinate Ni(II) porphyrins and found that following excitation these complexes relax to a $[3d_{z^2}, 3d_{x^2-y^2}]$ excited state, in which axial coordination can occur if amine ligands are available from coordinating solvents.^{11,12} Clearly, the axial

* Corresponding author. E-mail: andriy.kovalenko@nrc-cnrc.gc.ca.

[†] National Research Council of Canada.

[‡] Department of Chemical and Materials Engineering, University of Alberta.

[§] Department of Chemistry, University of Alberta.

^{||} Department of Mechanical Engineering, University of Alberta.

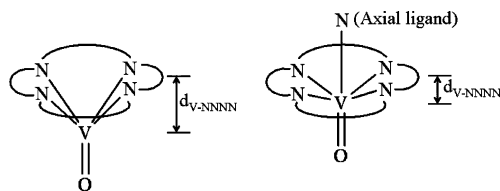


Figure 1. Schematic diagram of the square-pyramidal (left) and octahedral coordination of V in vanadyl porphyrins (right).

coordination is accompanied by a transition from a singlet to a triplet ground electronic state. Senge has suggested that axial coordination to Ni(II) porphyrins can be enhanced by peripheral electron-withdrawing group substitution and suppressed by nonplanar porphyrin macrocycles. He has demonstrated the success of this approach by synthesizing the 5,10,15,20-tetranitro-NiOEP (*m*-NiOEP) complex and characterizing it by X-ray crystallography.¹³

In vanadyl porphyrins, axial coordination is constrained by the geometrical arrangement of the V atom relative to the plane of the porphyrin N atoms due to the V=O bond, as we show in Figure 1. In vanadyl porphyrins, the V atom is displaced below the plane of the four porphyrin macrocycle N atoms by a distance d_{V-NNNN} , into a small cavity. For octahedral complex to be formed, the axial ligand has to reach the V atom situated in the cavity, which poses a severe steric constraint. Recently, the first crystal structure of a vanadyl octahedral complex that contains a pyridine ligand axially coordinated to 5,10,15,20-tetranitro-VOEP (*m*-VOEP) has been reported.¹⁴

Density functional theory (DFT) has become the preferred method for calculating a variety of molecular properties and has been successfully applied for understanding the electronic structure of molecular systems. However, transition metal complexes pose difficult challenges to DFT due to the nature of the metal–ligand bonding. Hybrid functionals that contain a small amount of exact Hartree–Fock exchange have been shown to be superior to nonhybrid functionals for both atomization energies¹⁵ and barrier heights¹⁶ of main group elements. Truhlar and co-workers have explored a set of 57 functionals, ranked these based on a comprehensive set of criteria, including metal–ligand and metal–metal binding energies as well as bond lengths, and found that the G96LYP functional performs the best.¹⁷ In another study, Zhao and Truhlar have ranked the PBE0 functional the best for nonbonded interactions and hydrogen bonding.¹⁸ It has been also shown that the PW91 functional is capable of modeling van der Waals interactions, although dispersive interactions are not physically included in it.¹⁹ In addition to functionals, DFT calculations require careful basis set selection because basis set size could produce different results, and even alter functional performance ranking, as demonstrated by Strassner and Taige for Gaussian-type basis sets.²⁰ For different basis set types, it has been reported that the double- ζ numerical basis set with polarization functions on H atoms (DNP) performs better than a Gaussian-type basis set of the same size, which is 6-31G**.^{21,22} Delley has shown that the PBE functional with DNP basis set correlates very well not only with the triple- ζ TNP basis set but also with the correlation-consistent cc-pVTZ basis set.²² Our experience has shown that using DFT requires careful and extensive functional exploration. In particular, for the strong noncovalent interaction in the streptavidin–biotin complex, we have found that binding energies calculated by using the PBE0 and MPW1B95 are in best agreement with the experiment.²³

Time-dependent DFT (TD-DFT) is a highly effective method for calculation of excited electronic states. This method has been

successfully employed for modeling of UV–vis absorption and emission spectra due to its high accuracy and applicability to relatively large structures.²⁴ The excited-state energies obtained by using the TD-DFT method coupled with the conductor-like polarizable continuum model (CPCM) of solvation correlate linearly with experimental UV–vis spectra, as we²⁵ and others have shown.^{26,27}

Reactivity indices provide a highly accurate insight in the binding interaction site preference prediction that comes at low computational cost.^{28,29} Fukui functions calculated using density functional theory (DFT) have been successfully applied for reactivity prediction in transition metal complexes,^{30,31} in particular for axial coordination of pyridine (py) to cobalt phthalocyanines.³² Fukui functions have been useful for adsorption preference prediction of aromatic fragments of large petroleum molecules, such as pyridines and thiophenes, on zeolite nanoparticles.^{33,34}

In this work, we present a computational exploration of the geometry, binding energy, and spectroscopic behavior of Ni(II) and vanadyl porphyrins in heavy oil. Moreover, the axial coordination and aggregation preferences of Ni(II) and vanadyl octaethyl porphyrins (NiOEP and VOOEP) toward petroleum fragments are analyzed by using Fukui functions and other reactivity indices. The predictions are supported by our spectroscopic results.

Computational Technique

For geometry optimization of the complexes, we have evaluated the performance of a semiempirical (PM6), the pure Hartree–Fock (HF), and several DFT methods. The semiempirical method PM6 includes the neglect of the diatomic differential overlap (NDDO), as implemented in the VAMP computational chemistry software.³⁵ The geometry optimization convergence was achieved when the gradient norm was lower than 1×10^{-1} kcal/(mol Å).

The functionals B3P86,^{36,37} B3PW91,^{36,38,39} BLYP,^{36,40} B3LYP,³⁸ G96LYP,^{40,41} X3LYP,^{40,42} O3LYP,^{40,43} MPW1B85,^{44,45} mPW1PW1,^{39,44} PBE (also called PBEPBE),⁴⁶ PBE0 (also called PBE1PBE),^{46,47} PW91 (also called PW91PW91),^{39,48,49} and TPSS (also called TPSSTPSS)⁵⁰ as well as the HF method⁵¹ that we study are implemented in the Gaussian 03 software.⁵² The all-electron double- ζ 6-31G* basis set is applied for all atoms.⁵³ The performance of the all-electron triple- ζ 6-311G* basis set⁵⁴ is also evaluated. A grid of 75 radial shells and 302 angular points per shell is used for numerical integrations of the two-electron integrals and their derivatives. The geometry optimization convergence is achieved when the energy, gradient, and displacement are lower than 1×10^{-6} Ha, 9×10^{-4} Ha/Å, and 1×10^{-3} Å, respectively.

For excited-state calculations, we employ the tandem of nonequilibrium TD-DFT^{27,55,56} and CPCM^{57,58} methods, as implemented in the Gaussian 03 software package,⁵² to produce a number of excited states in heptane solvent based on the ground-state geometries optimized in heptane by using the CPCM method. This tandem approach adds self-consistent reaction field around the solute and employs a linear response form for calculation of the excited states.^{57,59} For the complexes of the calibration series,⁶⁰ we perform geometry optimization in the gas phase and calculate excited states in chloroform solvent using the same methodology. The TD-DFT output contains information for the excited-state energies and oscillator strengths (f), and a list of the excitations that give rise to each excited state, the orbitals involved as well as the wave function

coefficients of the excitations. In this article, the excited states are presented as vertical bars with height equal to the oscillator strength.

We also evaluate the generalized gradient corrected BP,^{36,39} BLYP,^{36,39} VWN-BP,⁶¹ HCTH,⁶² PW91,⁴⁶ RPBE,^{46,63} and PBE⁴⁶ functionals, and the all-electron DNP basis set, as implemented in the DMol³ computational chemistry software that is integrated into the Accelrys Materials Studio 4.0 software suite.⁶⁵ We employ the extra-fine numerical integration grid that contains 474 angular points. The number of radial points is a function of the nuclear charge.⁶⁶ The geometry optimization convergence was achieved when the energy, gradient, and displacement were lower than 1×10^{-5} Ha, 1×10^{-3} Ha/Å, and 1×10^{-3} Å, respectively. In both Gaussian 03 and DMol³, the electronic singlet states are treated as single determinants, whereas the doublet and triplet states are treated as double determinants. The double determinant method is also referred to as unrestricted. We also test a method of thermal smearing of the orbital occupancy that is implemented in DMol³. It uses a finite-temperature Fermi function to compute fractional occupation numbers. The free energy A is calculated as

$$A = U_{\text{smear}} - TS \quad (1)$$

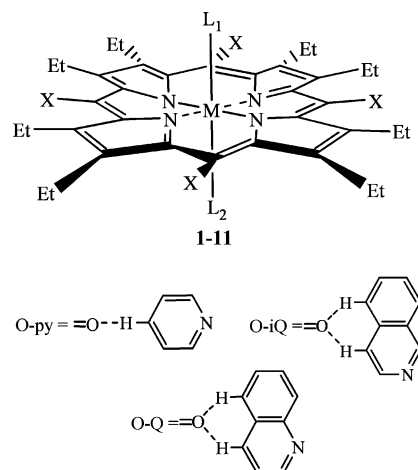
where U_{smear} is the electronic energy, T is the electronic temperature, and S is the entropy.⁶⁷

For the Fukui function calculations, we employ both Gaussian and DMol³. Noninteger total charge is implemented in DMol³ but not in Gaussian 03. In DMol³, we calculate Fukui functions for +0.1 lel and −0.1 lel charges, as noted below. In Gaussian 03, the Fukui functions are calculated for cations (+1.0 lel) and anions (−1.0 lel). The Fukui functions and electrostatic potentials calculated using DMol³ are in a good agreement with these calculated using Gaussian 03.

Results and Discussion

In Figure 2, we show schematic diagrams of the complexes included in this study. The pyridine (py), quinoline (Q), and isoquinoline (iQ) ligands are model fragments of large petroleum asphaltene molecules that belong to the archipelago structure model.⁸⁴ Complexes **1** and **2** contain four peripheral nitro groups that are thought to stabilize the axial metal–ligand bonds by withdrawing electron density from the porphyrin macrocycle and the metal atom. We use the structures of complexes **1** and **2**, resolved by X-ray crystallography and reported elsewhere, for validation of our computational methodology. Complexes **3–5** are square-pyramidal. Experimental evidence suggests that square-pyramidal Ni(II) complexes containing a piperidine ligand are more weakly bonded than the respective octahedral structures and have been detected in very low concentration.⁶⁸ Complexes **3–5** are too weakly bonded to be detected by UV–vis spectroscopy. These complexes could be nonbonded species. Complexes **6–8** are octahedral. These complexes have not been isolated as single crystals because the axial metal–ligand bonds are rather weak. For the interaction of VOOEP with the ligands, we consider both octahedral complexes and hydrogen-bonded aggregates (HBAs), labeled as **9–11** and **9'–11'**, respectively.

We have evaluated the performance of several computational methods with respect to geometry optimization and binding energies and found that the PW91 and PBE functionals implemented in DMol³ show the best performance. For ground electronic states, DFT functionals perform better than the HF



Complex	M	X	L ₁	L ₂
1	Ni	NO ₂	py	py
2	V	NO ₂	py	=O
3	Ni	-	py	-
4	Ni	-	iQ	-
5	Ni	-	Q	-
6	Ni	-	py	py
7	Ni	-	iQ	iQ
8	Ni	-	Q	Q
9/9'	V	-	py/-	=O/=O-py
10/10'	V	-	iQ/-	=O/=O-iQ
11/11'	V	-	Q/-	=O/=O-Q

Figure 2. Metalloporphyrin model systems.

TABLE 1: Atomic Charges (q_x), f_x^- , f_x^+ , and Global Softness (S) Values for Square-Planar Ni(II) Porphyrins, Square-Pyramidal Vanadyl Porphyrins, Pyridine (py), Quinoline (Q), and Isoquinoline (iQ) Calculated by Using the DMol³/PBE/DNP and Hirshfeld Population Analysis Methods^a

structure	S , Ha ^{−1}	q_x , lel	f_x^- , lel	f_x^+ , lel
NiOEP(s) (Ni)	18.00	0.119	0.199	0.020
NiOEP(t) (Ni)	26.26	0.310	0.063	0.176
VOOEP(d) (V)	20.02	0.360	0.105	0.012
VOOEP(d) (O)		−0.284	0.076	0.029
<i>tn</i> -NiOEP(s) (Ni)	22.73	0.129	0.124	0.011
<i>tn</i> -NiOEP(t) (Ni)	21.93	0.332	0.051	0.164
<i>tn</i> -VOOEP(d) (V)	25.56	0.360	0.098	0.008
<i>tn</i> -VOOEP(d) (O)		−0.264	0.069	0.021
py (N)	6.52	−0.165	0.297	0.156
Q (N)	8.25	−0.163	0.131	0.098
iQ (N)	8.92	−0.165	0.099	0.092

^a The values of q_x , f_x^- , and f_x^+ are given for the atom in parentheses.

and PM6 methods. For vertical electronic excited states, the TD-DFT/CPCM method implemented in Gaussian 03 yields excited states that correlate well with experimental UV–vis band energies and allow simulation of UV–vis spectra. Detailed method exploration results and discussion are included in the Supporting Information.

Binding Preference Prediction Methods. We predict the binding preferences of metalloporphyrins by using global softness, electrostatic potential (ESP) and Fukui functions. The global softness S is defined as follows:

$$S = 1/(\text{IP} - \text{EA}) \quad (2)$$

where IP is the ionization potential and EA is the electron affinity.⁶⁹ From the finite difference approximation for 0.1 lel we obtain

$$S = 0.1/[(E_{(N+0.1)} - E_{(N)} - E_{(N-0.1)})] \quad (3)$$

where $E_{N+0.1}$, E_N , and $E_{N-0.1}$ are the ground-state electronic energies of the system with charge of +0.1 lel, 0.0 lel, and -0.1 lel, respectively.

According to the hard and soft acid and base (HSAB) principle, a binding interaction between an acid A and a base B will be favored when the global softness difference ΔS , defined in eq 4, is minimal. This is obtained through optimization of the covalent contribution of the interaction energy, consequently neglecting other effects, such as polarization.⁷⁰

$$\Delta S = S_A - S_B \quad (4)$$

Chemical interactions have been categorized as being frontier orbital-controlled and charge-controlled.⁷¹ We employ two electron density derived functions Fukui functions and ESP to understand the axial coordination and aggregation preferences of NiOEP and VOOEP toward aromatic fragments of large petroleum molecules. The Fukui functions are applied for the prediction of orbital-controlled (soft-soft) interactions. The ESP shows the charge distribution around the molecule and is applied for the prediction of charge-controlled (hard-hard) interactions. However, it is difficult to establish threshold softness value and predict ligand coordination between reactants of intermediate softness.

The nucleophilic and electrophilic Fukui functions are defined in eqs 5 and 6, respectively. It is notable that there are similarities between the interpretation of the Fukui functions and the frontier molecular orbital theory proposed by Fukui.^{72,73} The electrophilic Fukui function maxima show the preferred sites for an attack by an electrophilic agent, whereas the nucleophilic Fukui function maxima show the preferred sites for an attack by a nucleophilic agent.

$$f_N^+(r) = (\delta\rho(r)/\delta N)_{v(r)}^+ = \rho_{N+0.1}(r) - \rho_N(r) \quad (5)$$

$$f_N^-(r) = (\delta\rho(r)/\delta N)_{v(r)}^- = \rho_N(r) - \rho_{N-0.1}(r) \quad (6)$$

In the finite difference approximation, for 0.1 lel the condensed Fukui functions⁷⁴ of atom x in a molecule that contains N electrons are defined in eqs 7 and 8.

$$f_x^+ = 10[q_x(N + 0.1) - q_x(N)] \quad (\text{for nucleophilic attack}) \quad (7)$$

$$f_x^- = 10[q_x(N) - q_x(N - 0.1)] \quad (\text{for electrophilic attack}) \quad (8)$$

From the viewpoint of the simplest molecular orbital theory model, additional electrons would occupy the lowest unoccupied molecular orbital (LUMO), whereas upon ionization electrons would be removed from the highest occupied molecular orbital (HOMO). Thus, it would be expected to some extent that f_N^+ and f_N^- be related to the LUMO and HOMO, respectively.

However, the Fukui function includes information not only about the frontier molecular orbitals but also about the orbital relaxation.

Coordination and Aggregation Preference Prediction.

In Table 1, we list the global softness and atomic Fukui function values of NiOEP, VOOEP, and the ligands, calculated by using the DMol³/PBE/DNP method. It is important to consider the lowest-lying triplet state of NiOEP because this helps to understand the formation of the octahedral complex, which is in a triplet ground state. For the complexes, the S values increase in the order NiOEP(s) < VOOEP(d) < NiOEP(t), where (s), (d), and (t) denote singlet ground, doublet ground, and triplet excited electronic states, respectively. For the ligands, the S values increase in the order py < Q < iQ. From the HSAB principle, the best softness match, i.e., the smallest softness difference (eq 4), would be preferred. The HSAB reactivity preferences increase in the order py-NiOEP(t) < Q-NiOEP(t) < iQ-NiOEP(t) < py-VOOEP < Q-VOOEP < iQ-VOOEP < py-NiOEP(s) < Q-NiOEP(s) < iQ-NiOEP(s). In Table 1, the larger of the f_x^+ and f_x^- values gives the predominant character of the atom x . For NiOEP(s), the higher f_{Ni}^- value relative to the f_{Ni}^+ value indicates that the Ni atom has a nucleophilic character. For NiOEP(t), the higher f_{Ni}^+ value relative to the f_{Ni}^- value indicates that the Ni atom has an electrophilic character. For the ligand N atoms, both the f_N^+ and f_N^- values increase in the order iQ < Q < py, which is opposite to the global softness increase order, indicating that softer molecules are more polarizable.

In Figure 3, we present the ESP and Fukui function maps that contain information on charge- and orbital-controlled bonding preferences, respectively. Color scale is available in the Supporting Information, Figure S10. In the top row, we show the ESPs of NiOEP, VOOEP, and the nitrogen-containing heterocyclic ligands. The ESP of NiOEP(s) plotted on the electron density surface does not have positive values near the Ni atom, indicating that this atom would be unreactive toward an attack by a ligand containing a negatively charged moiety. The absence of a positive charge on the Ni atom arises from the charge screening by the two electrons that occupy the d_{z^2} orbital. The ESP of NiOEP(t) has positive values near the Ni atom, indicating that NiOEP(t) would be reactive toward axial coordination. Thus, for axial coordination to occur, NiOEP (and all square-planar Ni complexes in the singlet ground state) must undergo a transition from singlet ground to triplet excited state. Upon excitation, one electron is promoted from the d_{z^2} to the $d_{x^2-y^2}$ orbital of Ni(II).^{11,12,75} Details on the singlet and triplet state coordination to NiOEP are available in the Supporting Information.

For VOOEP, the ESP values near the V atom are positive, whereas the values near the O atom are negative. Thus, the V atom is preferred for an attack by negatively charged ligand moieties, whereas the O atom is preferred for an attack by positively charged moieties. For comparison, we also optimize the geometry of VOOEP in the lowest-lying quartet excited state. We examined the ESP and Fukui function maps and found that these have qualitatively the same character as VOOEP(d). The ligand ESP maps show large negative values near the N atoms, indicating that these atoms are preferred for attack by positively charged moieties.

In Figure 3 (middle and bottom rows), we show the Fukui functions of NiOEP, VOOEP, and the axial ligands, mapped on the electron density surfaces. The Fukui function maxima and minima are shown in red and blue, respectively. For NiOEP(s), the f^- maximum is near the Ni atom, indicating increased reactivity preference of this atom toward an electro-

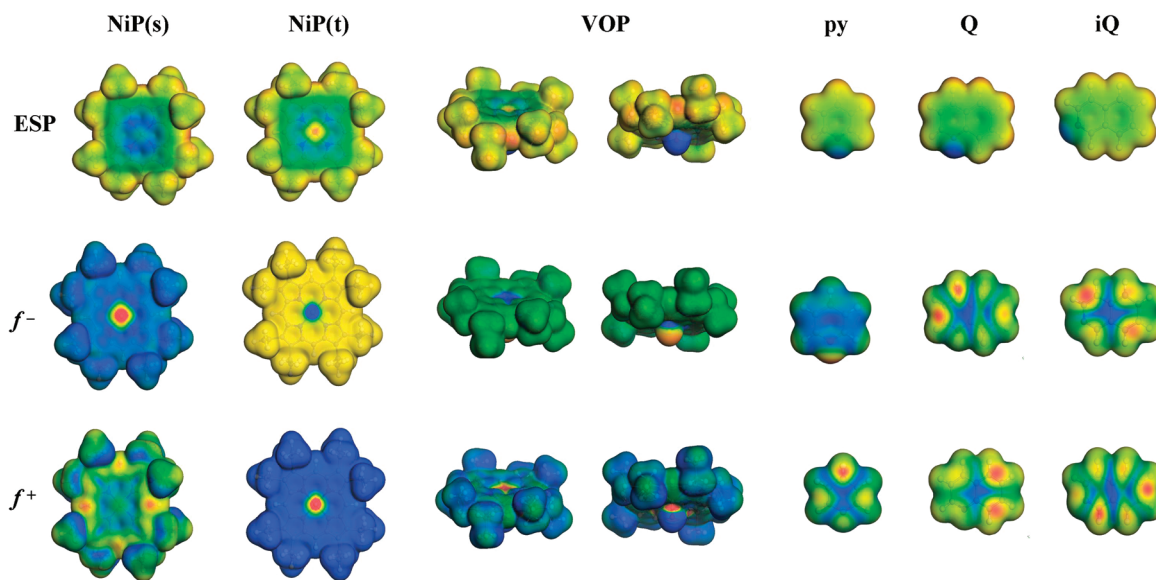


Figure 3. Electrostatic potential (ESP), electrophilic (f^-), and nucleophilic (f^+) Fukui functions of NiOEP(s), NiOEP(t), VOOEP, and ligands mapped on the $0.017 \text{ e}/\text{\AA}^3$ electron density surface calculated by using the DMol³/PBE/DNP method. The ESP, f^- , and f^+ minima to maxima values are mapped in blue to red colors, respectively. Color scales are available in the Supporting Information, Figure S1.

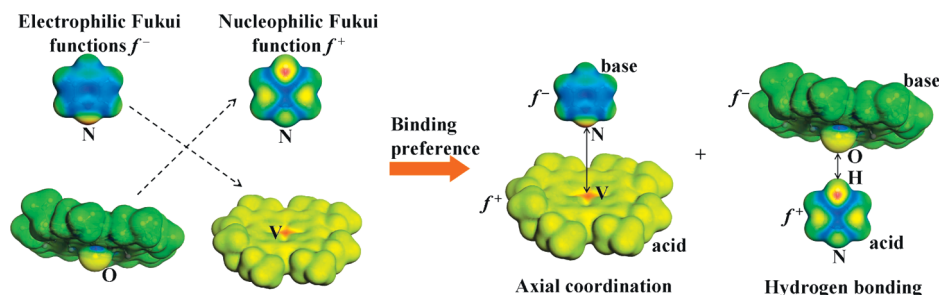


Figure 4. Binding preference prediction scheme for VOOEP and pyridine based on Fukui functions mapped on the $0.017 \text{ e}/\text{\AA}^3$ electron density surface, calculated by using the DMol³/PBE/DNP method. The f^- and f^+ minima to maxima values are mapped in blue to red colors, respectively.

philic attack. The f^+ maxima are at the methine C atoms located at the 5 and 15 porphyrin positions, indicating increased reactivity of these atoms toward a nucleophilic attack. The Fukui function results are in agreement with the ESP results in showing that NiOEP(s) is unreactive toward axial coordination. For NiOEP(t), the maximum of f^- is not localized. In both the f^+ map of NiOEP(t) and the f^- map of NiOEP(s) the maxima are near the Ni atoms. For NiOEP(t), the Fukui functions allow to clearly predict that the Ni atom is the preferred site for axial coordination by nucleophiles, such as nitrogen-containing heterocyclic ligands.

The ligand Fukui functions have been investigated previously.⁷⁶ For py, the f^- maximum is near the N atom. For Q and iQ, the f^- maxima are near C and H atoms. For all three ligands, the f^+ maxima are near C and H atoms. For Q and iQ, the Fukui functions suggest different reactivity preferences from the ESP because the next to the highest occupied molecular orbital (HOMO-1) has an N atom lone-pair character. For py, the HOMO has an N atom lone-pair character. For Q and iQ, the orbital relaxation results suggest that the HOMO-1 is not involved in an electrophilic attack. The ligand Fukui functions indicate that only the N atom of py is preferred for electrophilic attack by NiOEP and VOOEP.

In order to predict binding preferences, we match the maxima of the Fukui functions and ESP for pairs of reactants. In Figure 4, we present the binding preference prediction scheme for the

pair VOOEP-py based on the Fukui functions. The nucleophilic and electrophilic Fukui function maps are cross-matched, as we show in Figure 4 (left) in dotted arrows, to obtain two pairs of Fukui functions. By matching of the f^+ and f^- maxima for both py and VOOEP, we determine that the electrophilic V atom is the preferred site for axial coordination of the py ligand, whereas the nucleophilic O atom is the preferred site for hydrogen bonding of py. This result suggests two types of binding interaction between VOOEP and py. First, VOOEP is assigned as a base and py is assigned as an acid. We visually examine the f^- map of VOOEP and the f^+ map of py, and place the maxima next to each other. Thus, a hydrogen bond would form between the O atom of VOOEP and the H atom at the 4-position of py. This product is the HBA 9' (Figure 2). Second, VOOEP is assigned as an acid and py is assigned as a base. We examine the f^+ map of VOOEP and the f^- map of py, and find that an axial coordination bond would form between the N atom of py and the V atom of VOOEP. The product is the octahedral complex 9. For the two cases considered, we construct structures 9 and 9' and perform full geometry optimization to compare the total energies of these adducts.

In Figure 5, we present the ESP matching scheme for the pair of py and VOOEP. The ESP values of VOOEP are positive near the V atom and the methine linker H atoms, and negative near the O atom. Some negative charge is also smeared on the porphyrin macrocycle. The ESP values of py are positive near

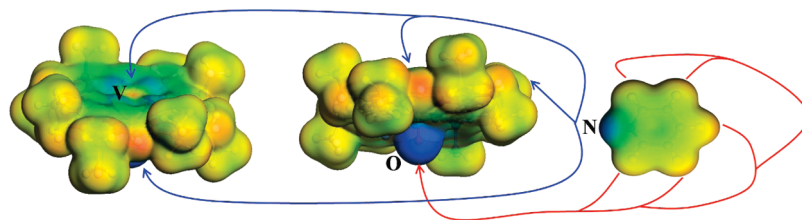


Figure 5. Aggregation preference prediction scheme for VOOEP and pyridine based on ESP mapped on the $0.017 \text{ e}/\text{\AA}^3$ electron density surface, calculated by using the DMol³/PBE/DNP method. The ESP minima to maxima values are mapped in blue to red colors, respectively. Red lines and arrows show the binding preferences of py based on the H atom sites. Blue lines and arrows show the binding preferences of py based on the N atom site.

TABLE 2: Metal–Ligand (M–L_{AX}) and Hydrogen Bond Lengths (O–H_{HBA}), Axial (E_b^{Ax}) and Hydrogen-Bonding Energies (E_b^{HB}) for Complexes 1–11 Optimized by Using DMol³/PW91/DNP and DMol³/PBE/DNP Methods^a

functional	1	2	3	4	5	6	7	8	9/9'	10/10'	11/11'
				M–L _{AX} (D _A)/O–H _{HBA} , Å							
PW91/DNP	2.21 (0.00)	2.62 (0.13)/2.36	2.08	2.08	2.18	2.23	2.24	2.67	2.68/2.26	2.66/2.49	3.39/2.49
PBE/ DNP	2.23 (0.02)	2.62 (0.13)/2.36	2.09	2.09	2.20	2.23	2.24	2.57	2.68/2.26	2.67/2.49	3.43/2.55
				$E_b^{\text{Ax}}/E_b^{\text{HB}}$, kJ/mol							
PW91/DNP	−37	−44/−18	+22	+17	+41	−17	−25	+65	−25/−22	−27/−28	−17/−27
PBE/DNP	−44	−40/−16	+17	+8	+33	−24	−40	+5	−21/−20	−23/−25	−13/−24

^a The absolute deviations of the optimized bond lengths for complexes **1** and **2** from the experimental X-ray crystallography values of 2.206 and 2.495 Å, respectively, are denoted as D_A and listed in parentheses.

the H atoms and negative near the N atom. For py, the preferred binding with respect to the H atoms leads to formation of hydrogen bonds to the O atom of VOOEP. The preferred binding with respect to the N atom leads to the formation of an axial coordination bond to the V atom and a hydrogen bonds to the methine H atoms. The ESP matching produces several more adducts than the Fukui function matching but these are less stable. Similarly, we construct octahedral complexes and HBAs for Q-VOOEP and iQ-VOOEP, and optimize these geometries. It is important to note that the reactivity preferences predicted from ΔS , Fukui functions, and ESP do not take into account steric factors because these are based only on the reactant structures. Also, the predictions are more successful for rigid reactants, where the geometry changes upon binding are small.

The reactivity preference analysis also suggests that the dimer of VOOEP(d) would be a preferred aggregate. From the ΔS , ESP, and Fukui function analysis, we expect that this aggregate would be stable. However, the VOOEP dimer stability is dramatically reduced by the peripheral ethyl group steric crowding. We analyze the ESP and Fukui functions of vanadyl porphine and find that these are qualitatively very similar to those of VOOEP, suggesting that the vanadyl porphine could form a stable dimer.

For the peripherally substituted *m*-NiOEP and *m*-VOOEP, the data in Table 3 shows rather small changes relative to NiOEP and VOOEP, respectively. Despite the presence of electron-withdrawing groups, the V atom charge does not increase and the Ni atom charge increases by 0.02 lel. The atomic Fukui functions show reduced, instead of increased, reactivity of the metal atom. This is due to the greater deviation of the porphyrin macrocycle from planarity and the more efficient screening of the V atom by the pyrrole N atoms and the vanadyl group O atom in *m*-VOOEP. As our geometry optimization results show, the $d_{\text{V-NNN}}$ is larger in *m*-VOOEP than in VOOEP, thus the V atom is less accessible for axial coordination. This geometry change is reflected in the electron density and charge distribution and the V atom charge is smeared on the nearest neighbor atoms.

Geometry Optimization of Complexes 3–11. In Table 2, we list the metal–ligand bond lengths of the complexes obtained by full geometry optimization in the gas phase by using the

PBE and PW91 functionals, as implemented in DMol³. For complexes **3–5**, we obtain shorter Ni–N(axial) bond length relative to complexes **6–8**, respectively, despite that in complexes **3–5** the axial bonds are weaker. This is due to the enhanced accessibility of the Ni atom in the square-pyramidal coordination environment. In complex **7**, the metal–axial ligand bond length increases by 0.01 Å relative to complex **6**, whereas for the vanadyl analogues, the trend is opposite. The very long axial bond obtained for complex **8** is due to the steric hindrance of the H atom at the 8 position in the Q ligand.

For VOOEP, our PBE/DNP geometry optimization results show that the $d_{\text{V-NNN}}$ is 0.52 Å, in excellent agreement with the X-ray crystallographic determination.⁷⁷ For complexes **9** and **10**, the $d_{\text{V-NNN}}$ value decreases to 0.36 Å. For complex **2**, the $d_{\text{V-NNN}}$ decreases from 0.55 to 0.35 Å upon axial coordination. The latter value is longer than the experimental $d_{\text{V-NNN}}$ of 0.29 Å.¹⁴ The difference can be attributed to crystal packing. Comparison between the changes in the $d_{\text{V-NNN}}$ shows that upon peripheral substitution with electron-withdrawing groups the $d_{\text{V-NNN}}$ decreases by 0.20 Å for complex **2** relative to 0.16 Å for complex **9**, rendering the V atom of complex **2** more accessible to axial coordination. These results show that the steric accessibility of the V atom is more important for axial coordination than the mere peripheral substituent electronic effect.

The hydrogen-bonding aggregation configuration between VOOEP and nitrogen-containing heterocyclic ligands suggested by our reactivity preference analysis is particularly interesting. For complexes **9'–11'**, the hydrogen bonds are rather long, as expected for H atoms in aromatic systems. The only direct observation of hydrogen bonding between two aromatic H atoms of pyrene and an ethyl formate carbonyl group O atom on Pt(111) surface is presented by Lavoie et al. from scanning tunneling microscopy (STM) studies. These authors report a hydrogen bond length estimate of $1.8 \pm 0.1 \text{ Å}$.⁷⁸

Binding Energies. In Table 2, we also list the binding energies of complexes **1–11** obtained by using the PBE0 and PW91 functionals, as implemented in DMol³. The binding energies of the complexes are calculated relative to optimized uncoordinated (*m*-) NiOEP, (*m*-) VOOEP, and ligands as follows:

$$E_b = (E_{C_x} - mE_L - E_{sqP})/m \quad (9)$$

where E_{C_x} is the total energy of a complex **1–11** and E_L is the total energy of a ligand, all in the respective ground electronic states. The E_{sqP} is the total energy of the square-planar (*m*-) NiOEP or square-pyramidal (*m*-) VOOEP, and m is the number of ligands in a complex of the series **1–11**. The binding energies E_b are specified as E_b^{Ax} and E_b^{HB} for axial coordination and hydrogen bonding, respectively.

For complexes **6** and **7**, the E_b^{Ax} values indicate that the coordination strength of the iQ ligand is higher than that of the py ligand. For complexes **9** and **10**, the E_b^{Ax} show that the ligand coordination strength is the same, whereas for complex **11** the coordination strength is lower by ~ 10 kJ/mol. Clearly, the N atoms in py and iQ are almost equally accessible to coordination, whereas the N atom of Q is less accessible due to the steric hindrance caused by the H atom at the 8 position. Therefore, the coordination to VOOEP is determined primarily by the ability of the ligand to access the metal center.

For the vanadyl porphine dimer in the triplet ground state, we obtain an aggregation energy value of -8 kJ/mol. It would be interesting to find out whether vanadyl porphine forms 1D stacked structures in solid state. Unfortunately, the crystal structure of vanadyl porphine has not been reported. We have also considered an octahedral complex that contains a py ligand on the same face of VOOEP(d) as the oxo- ligand and found that this structure is not bound.

For complex **2**, the E_b^{HB} is lower than E_b^{Ax} , whereas for complex **11** it is the opposite. For complexes **9** and **10** these values are comparable. The stabilization of the HBA aggregates relative to the respective octahedral complexes is due to the steric freedom near the O atom and the formation of two hydrogen bonds in each complex involving the H atoms at the 4 and 5 positions of Q and iQ (Figure 2). These results suggest that HBA could compete with axial coordination. Such HBA structures have not been previously identified as relevant to asphaltene aggregation.

Formation Constants. We verify experimentally the coordination preference predictions by exploring the axial binding of NiOEP and VOOEP using visible absorption spectroscopy. The formation constants for py-NiOEP, iQ-NiOEP, py-VOOEP, and iQ-VOOEP are 0.03 ± 0.01 , 0.12 ± 0.03 , 0.15 ± 0.02 , and 0.23 ± 0.03 , respectively. These values were determined in hexane solvent by spectrophotometric titration following the decrease of the Soret bands of VOOEP and NiOEP upon addition of py and iQ ligands.⁷⁹ The formation constant values show that the vanadyl complexes are more inert than the respective Ni(II) complexes. Also, complexes that contain iQ ligand are more inert than those containing py ligand. The formation constant increase order is in agreement with the axial coordination preference order based on global softness matching, except for NiOEP(s) (vide supra). Our formation constant values for axial coordination to VOOEP compare favorably to these reported in the literature.⁸⁰ The spectrophotometric titration data is available in the Supporting Information, Figures S7–S10.

Excited States and UV–Vis Spectra. The simulated excited-state energies and experimental visible adsorption band energies are listed in Table 3. In Figure 6, we show the appearance of a higher energy band upon addition of py and iQ to VOOEP overlaid with the simulated excited-state energies for complexes **9**, **10**, and VOOEP. For complex **9**, the agreement between experiment and theory is impressive. Considering the low formation constant of complex **9**, the assignment of the shoulder at 422 nm to its Soret band is very reasonable. Bonnett et al.

TABLE 3: Simulated Excited-State (λ_{ES}) and Experimental Visible Adsorption Band (λ_{Exp}) Wavelengths in Heptane Solvent^a

complex	Soret band		α band	
	λ_{ES} , nm	λ_{Exp} , nm	λ_{ES} , nm	λ_{Exp} , nm
NiOEP(s)	393	392	543	551
VOOEP(d)	407	406	565	566
3	408	—	511	—
4	408	—	511	—
5	408	—	511	—
6	415	—	570	—
7	413	—	570	—
8	410	—	564	—
9/9'	424	408, 422(sh)	580	571
10/10'	426	411, 425(sh)	581	573
11/11'	389	—	568	—

^a The λ_{ES} values are calculated by using the G03/PBE0/6-31G* method. sh = shoulder, $\lambda_{ES} = 1240/E_{ES}$.

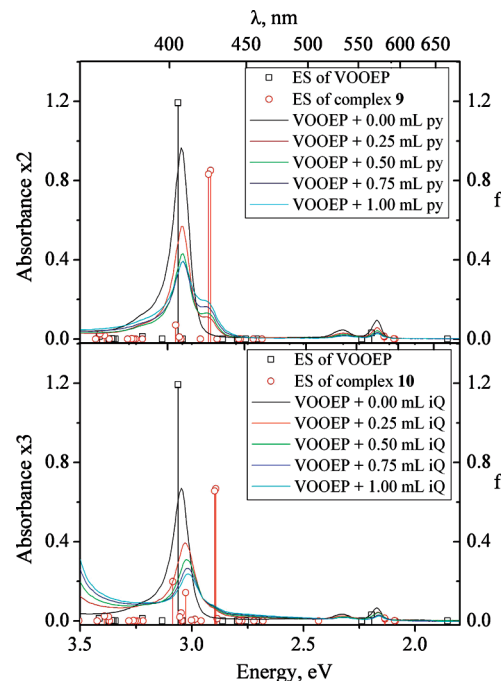


Figure 6. Visible spectrum of VOOEP in 0.5 mL of heptane ($1.5 \mu\text{M}$) with addition of 0.25–1.00 mL of pure (12.4 M) pyridine (top) and isoquinoline (bottom) as well as simulated excited states (ES) of VOOEP and complexes **9** and **10** presented as vertical bars with height equal to the oscillator strength (f), calculated by using the G03/PBE0/6-31G* method.

report, however, that for axial coordination of py to VOOEP the Soret band of complex **9** is split.⁶⁰ The resonance Raman spectra of VOOEP in pyridine solvent contain two $\text{V}=\text{O}$ bands that have been attributed to VOOEP and complex **9**.⁸¹ Upon spectrophotometric titration of VOOEP with iQ, the Soret band is shifted from 407 to 411 nm, which is smaller than the shift from 407 to 421 nm predicted in our calculations for complex **10**. This result could be due to the spectral broadening caused by the excited states at 3.0–3.1 eV that have relatively high oscillator strength. Such states are absent in complex **9**. The experimentally observed shifts upon addition of Q to VOOEP as well as py, iQ, and Q to NiOEP are negligible. The Soret band excited-state energies of HBAs are not shifted relative to VOOEP, and thus the presence of HBAs cannot be confirmed by visible spectroscopy. Our Soret band correlations from TD-DFT and visible spectroscopy are in agreement with our E_b^{Ax}

and E_b^{HB} results in showing that Q axial coordination might not occur. These results are consistent with the suggestion that establishing correlations between simulated and experimental spectroscopic data could be a more reliable approach for structure determination than geometry optimization alone.⁸²

Our future work will involve enhancing of the axial coordination preference of VOOEP by porphyrin system modification, developing a reactivity prediction methodology based on matching the shapes of ESP and Fukui function surfaces, as well as implementing a tandem of the three-dimensional reference interaction site model (3D-RISM) statistical-mechanical theory of solvation⁸³ and the TD-DFT method. This implementation will allow excited state calculation in solution, where the solvent is described with accuracy comparable to explicit solvation at much lower computational cost.

Conclusion

We have evaluated the performance of several advanced computational methods for prediction of the optimized geometries, binding energies, and excited states of Ni(II) and vanadyl porphyrins relevant to aggregates formed in petroleum. Our results show that the PBE and PW91 functionals, as implemented in the DMol³ software, predict the optimized geometries of Ni(II) and vanadyl porphyrins but overestimate the V–N(axial) bond length. The axial binding energy comparison allows estimation of a threshold between strongly, weakly, and not bound complexes, and shows that the PBE and PW91 functionals in combination with the DNP basis set perform better than the commonly used B3LYP functional for bond lengths and binding energies. Linear correlation between the excited-state energies calculated by using the TD-DFT/CPCM method and experimental absorption band energies is established for the PBE0 and B3LYP functionals, and employed for the simulation of the excited-state energies of weakly bonded complexes. For excited-state calculations, the PBE0 and B3LYP functionals provide comparable quality. The simulated excited-state energies are in agreement with our UV–vis spectrophotometric studies and the Soret band assignment for axial coordination of py and iQ to VOOEP. These results increase the understanding of the Soret band broadening in porphyrins relevant to petroleum.

Analysis of the preferences of NiOEP and VOOEP toward axial coordination of nitrogen-containing heterocyclic ligands by using a set of reactivity prediction methods shows that NiOEP(t) has high preference toward axial coordination, whereas NiOEP(s) is unreactive. The binding preference order based on global softness matching is in agreement with the experimental formation constant order. Our results show that the axial coordination to VOOEP is controlled primarily by steric factors, in particular, the accessibility of the V atom. The binding preference prediction schemes for the interaction between VOOEP and py based on Fukui function cross-matching and ESP matching allow identification of hydrogen-bonded aggregates as new species relevant to heavy oils and bitumen.

Acknowledgment. Funding in support of this research is provided by the Imperial Oil-Alberta Ingenuity Centre for Oil Sands Innovation (COSI) at the University of Alberta, Natural Sciences and Engineering Research Council (NSERC) of Canada, and National Research Council (NRC) of Canada. The computations are supported by the Western Canada Research Grid (WestGrid) as well as by the Centre for Excellence in Integrated Nanotools (CEIN) and the Academic Information and Communication Technologies (AICT) servers at the University

of Alberta. The authors thank Dr. Robert McDonald, Service Crystallographer in the Department of Chemistry at the University of Alberta, for his support with the access to the Cambridge Crystallography Data Centre (CCDC). The authors also thank Dr. John M. Villegas for his discussion and suggestions on the presentation of the results. M.G. holds a Canada Research Chair.

Supporting Information Available: Computational method exploration results and discussion, spectrophotometric titration, and excited-states data. This material is available free of charge via the Internet at <http://pubs.acs.org>.

References and Notes

- (1) Yen, T. F. *Role Trace Met. Pet.* **1975**, *1*, 30.
- (2) Filby, R. H. *Role Trace Met. Pet.* **1975**, *31*, 58.
- (3) Treibs, A. *Liebigs. Ann.* **1934**, *509*, 103 Ibid. 510, 42.
- (4) (a) Callot, H. J.; Ocampo, R. In *The Porphyrin Handbook*; Kadish, K. M., Smith, K. M., Guillard, R., Eds.; Academic Press: New York, 2000; Vol. 1, p 349; (b) Czernuszewicz, R. S. *J. Porphyrins Phthalocyanines* **2000**, *4*, 426. (c) Kashiyama, Y.; Shiro, M.; Tada, R.; Ohkouchi, N. *Chem. Lett.* **2007**, *36*, 706.
- (5) Smith, K. M. *Porph. Metalloporph.* **1975**, *3*, 28.
- (6) Sugihara, J. M.; Bean, R. M. *J. Chem. Eng. Data* **1962**, *7*, 269–271.
- (7) Dickie, J. P.; Yen, T. F. *Anal. Chem.* **1967**, *39*, 1847–52.
- (8) Yin, C.-X.; Tan, X.; Mullen, K.; Stryker, J. M.; Gray, M. *Energy Fuels* **2008**, *22*, 2465–2469.
- (9) Qian, K.; Mennito, A. S.; Edwards, K. E.; Ferrughelli, D. T. *Rapid Commun. Mass Spectrom.* **2008**, *22*, 2153–2160.
- (10) Caughey, W. S.; Deal, R. M.; McLees, B. D.; Alben, J. O. *J. Am. Chem. Soc.* **1962**, *84*, 1735.
- (11) (a) Kim, D. H.; Kirmaier, C.; Holten, D. *Chem. Phys.* **1983**, *75*, 305. (b) Findsen, E. W.; Shellnut, J. A.; Freidman, J. M.; Ondaris, M. R. *Chem. Phys. Lett.* **1983**, *98*, 584.
- (12) Rodriguez, J.; Holten, D. *J. Chem. Phys.* **1990**, *92*, 5944–5950.
- (13) Senge, M. O. *J. Porphyrins Phthalocyanines* **1998**, *2*, 107.
- (14) Ghosh, S. K.; Patra, R.; Rath, S. P. *Inorg. Chem.* **2008**, *47*, 9848.
- (15) Becke, A. D. *J. Chem. Phys.* **1993**, *98*, 5648.
- (16) Zhao, Y.; Truhlar, D. G. *J. Phys. Chem. A* **2005**, *109*, 5656.
- (17) Schultz, N. E.; Zhao, Y.; Truhlar, D. G. *J. Phys. Chem. A* **2005**, *109*, 11127–11143.
- (18) Zhao, Y.; Truhlar, D. G. *J. Chem. Theory Comput.* **2005**, *1*, 415–432.
- (19) (a) Tsuzuki, S.; Luthi, H. P. *J. Chem. Phys.* **2001**, *114*, 3949. (b) Johnson, E. R.; Wolkow, R. A.; DiLabio, G. A. *Chem. Phys. Lett.* **2004**, *394*, 334–338.
- (20) Strassner, T.; Taige, M. A. *J. Chem. Theory Comput.* **2005**, *1*, 848–855.
- (21) Inada, Y.; Orita, H. *J. Comput. Chem.* **2007**, *29*, 225.
- (22) Delley, B. *J. Phys. Chem. A* **2006**, *110*, 13632–13639.
- (23) Li, Q.; Gusarov, S.; Evoy, S.; Kovalenko, A. *J. Phys. Chem. C* **2009**, *113*, 9958–9967.
- (24) (a) Monat, J. E.; Rodriguez, J. H.; McCusker, J. K. *J. Phys. Chem. A* **2002**, *106*, 7399. (b) Rodriguez, J. H.; Wheeler, D. E.; McCusker, J. K. *J. Am. Chem. Soc.* **1998**, *120*, 12051. (c) Stoyanov, S. R.; Villegas, J. M.; Rillema, D. P. *Inorg. Chem.* **2003**, *42*, 7852. (d) Stoyanov, S. R.; Villegas, J. M.; Cruz, A. J.; Lockyear, L. L.; Reibenspies, J. H.; Rillema, D. P. *J. Chem. Theory Comput.* **2005**, *1*, 95–106.
- (25) Stoyanov, S. R.; Villegas, J. M.; Rillema, D. P. *Inorg. Chem. Commun.* **2004**, *7*, 838.
- (26) Kozłowski, P. M.; Kuta, J.; Ohta, T.; Kitagawa, T. *J. Inorg. Biochem.* **2006**, *100*, 744.
- (27) Casida, M. E.; Jamorski, C.; Casida, K. C.; Salahub, D. R. *J. Chem. Phys.* **1998**, *108*, 4439.
- (28) Roy, R. K.; Krishnamurti, S.; Geerlings, P.; Pal, S. *J. Phys. Chem. A* **1998**, *102*, 3746.
- (29) Deka, R. Ch.; Roy, R. K.; Hirao, K. *Chem. Phys. Lett.* **2004**, *389*, 186.
- (30) Cardenas-Jiron, G. I.; Venegas-Yazigi, D. A. *J. Phys. Chem. A* **2002**, *106*, 11938.
- (31) Cardenas-Jiron, G. I.; Caro, C. A.; Venegas-Yazigi, D.; Zagal, J. H. *J. Mol. Struct. Theochem* **2002**, *580*, 193.
- (32) Cardenas-Jiron, G. I. *Int. J. Quantum Chem.* **2003**, *91*, 389–397.
- (33) Stoyanov, S. R.; Gusarov, S.; Kuznicki, S. M.; Kovalenko, A. *J. Phys. Chem. C* **2008**, *112*, 6794–6810.
- (34) Stoyanov, S. R.; Gusarov, S.; Kovalenko, A. *Mol. Simul.* **2008**, *34*, 943–951.

- (35) (a) Stewart, J. J. P. *J. Mol. Model.* **2007**, *13*, 1173. (b) Pople, J. A.; Santry, D. P. *J. Chem. Phys.* **1965**, *43*, S129.
- (36) Becke, A. D. *Phys. Rev. A* **1988**, *38*, 3098.
- (37) Perdew, J. P. *Phys. Rev. B* **1986**, *33*, 8822.
- (38) Becke, A. D. *J. Chem. Phys.* **1993**, *98*, 5648–5652.
- (39) Perdew, J. P. In *Electronic Structure of Solids '91*; Ziesche, P., Eschling, H., Eds.; Akademie Verlag: Berlin, Germany, 1991; p 11.
- (40) Lee, C.; Yang, W.; Parr, R. G. *Phys. Rev. B* **1988**, *37*, 785–789.
- (41) Gill, P. M. W. *Mol. Phys.* **1996**, *89*, 433.
- (42) (a) Xu, X.; Goddard III, W. A. *Proc. Natl. Acad. Sci.* **2004**, *101*, 2673. (b) Xu, X.; Zhang, Q.; Muller, R. P.; Goddard III, W. A. *J. Chem. Phys.* **2005**, *122*, 014105.
- (43) (a) Handy, N. C.; Cohen, A. J. *Mol. Phys.* **2001**, *99*, 403. (b) Wilson, P. J.; Bradley, T. J.; Tozer, D. J. *J. Chem. Phys.* **2001**, *115*, 9233.
- (44) Adamo, C.; Barone, V. *J. Chem. Phys.* **1998**, *108*, 664.
- (45) (a) Becke, A. D. *J. Chem. Phys.* **1996**, *104*, 1040. (b) Zhao, Y.; Gonzalez-Garcia, N.; Truhlar, D. G. *J. Phys. Chem. A* **2005**, *109*, 2012.
- (46) (a) Perdew, J. P.; Burke, K.; Ernzerhof, M. *Phys. Rev. Lett.* **1996**, *77*, 3865. (b) Perdew, J. P.; Burke, K.; Ernzerhof, M. *Phys. Rev. Lett.* **1997**, *78*, 1396E.
- (47) (a) Adamo, C.; Cossi, M.; Barone, V. *THEOCHEM* **1999**, *493*, 145. (b) Ernzerhof, M.; Scuseria, G. E. *J. Chem. Phys.* **1999**, *110*, 5029.
- (48) (a) Perdew, J. P.; Chevary, J. A.; Vosko, S. H.; Jackson, K. A.; Pederson, M. R.; Singh, D. J.; Fiolhais, C. *Phys. Rev. B* **1992**, *46*, 6671–6687. (b) Perdew, J. P.; Chevary, J. A.; Vosko, S. H.; Jackson, K. A.; Pederson, M. R.; Singh, D. J.; Fiolhais, C. *Phys. Rev. B* **1993**, *48*, 4978.
- (49) (a) Perdew, J. P.; Burke, K.; Wang, Y. *Phys. Rev. B* **1996**, *54*, 16533. (b) Burke, K.; Perdew, J. P.; Wang, Y. In *Electronic Density Functional Theory: Recent Progress and New Directions*; Dobson, J. F., Vignale, G., Das, M. P., Eds.; Plenum: New York, 1998.
- (50) Tao, J.; Perdew, J. P.; Staroverov, V. N.; Scuseria, G. E. *Phys. Rev. Lett.* **2003**, *91*, 146401.
- (51) (a) Roothaan, C. C. J. *Rev. Mod. Phys.* **1951**, *23*, 69. (b) Pople, J. A.; Nesbet, R. K. *J. Chem. Phys.* **1954**, *22*, 571–72. (c) McWeeny, R.; Dierksen, G. *J. Chem. Phys.* **1968**, *49*, 4852.
- (52) Frisch, M. J.; Trucks, G. W.; Schlegel, H. B.; Scuseria, G. E.; Robb, M. A.; Cheeseman, J. R.; Montgomery, Jr., J. A.; Vreven, T.; Kudin, K. N.; Burant, J. C.; Millam, J. M.; Iyengar, S. S.; Tomasi, J.; Barone, V.; Mennucci, B.; Cossi, M.; Scalmani, G.; Rega, N.; Petersson, G. A.; Nakatsuji, H.; Hada, M.; Ehara, M.; Toyota, K.; Fukuda, R.; Hasegawa, J.; Ishida, M.; Nakajima, T.; Honda, Y.; Kitao, O.; Nakai, H.; Klene, M.; Li, X.; Knox, J. E.; Hratchian, H. P.; Cross, J. B.; Bakken, V.; Adamo, C.; Jaramillo, J.; Gomperts, R.; Stratmann, R. E.; Yazyev, O.; Austin, A. J.; Cammi, R.; Pomelli, C.; Ochterski, J. W.; Ayala, P. Y.; Morokuma, K.; Voth, G. A.; Salvador, P.; Dannenberg, J. J.; Zakrzewski, V. G.; Dapprich, S.; Daniels, A. D.; Strain, M. C.; Farkas, O.; Malick, D. K.; Rabuck, A. D.; Raghavachari, K.; Foresman, J. B.; Ortiz, J. V.; Cui, Q.; Baboul, A. G.; Clifford, S.; Cioslowski, J.; Stefanov, B. B.; Liu, G.; Liashenko, A.; Piskorz, P.; Komaromi, I.; Martin, R. L.; Fox, D. J.; Keith, T.; Al-Laham, M. A.; Peng, C. Y.; Nanayakkara, A.; Challacombe, M.; Gill, P. M. W.; Johnson, B.; Chen, W.; Wong, M. W.; Gonzalez, C.; Pople, J. A. *Gaussian 03, Revision C.02*; Gaussian, Inc.: Wallingford, CT, 2004.
- (53) Hehre, W. J.; Ditchfield, R.; Pople, J. A. *J. Chem. Phys.* **1972**, *56*, 2257.
- (54) (a) McLean, A. D.; Chandler, G. S. *J. Chem. Phys.* **1980**, *72*, 5639. (b) Krishnan, R.; Binkley, J. S.; Seeger, R.; Pople, J. A. *J. Chem. Phys.* **1980**, *72*, 650.
- (55) Stratmann, R. E.; Scuseria, G. E.; Frisch, M. J. *J. Chem. Phys.* **1998**, *109*, 8218.
- (56) Bauernschmitt, R.; Ahlrichs, R. *Chem. Phys. Lett.* **1996**, *256*, 454.
- (57) Cossi, M.; Barone, V. *J. Chem. Phys.* **2001**, *115*, 4708.
- (58) (a) Barone, V.; Cossi, M. *J. Phys. Chem. A* **1998**, *102*, 1995. (b) Cossi, M.; Rega, N.; Scalmani, G.; Barone, V. *J. Comput. Chem.* **2003**, *24*, 669.
- (59) Cammi, R.; Mennucci, B.; Tomasi, J. *J. Phys. Chem. A* **2000**, *104*, 5631–5637.
- (60) Bonnett, R.; Brewer, P.; Noro, K.; Noro, T. *Tetrahedron* **1978**, *34*, 379–385.
- (61) Vosko, S. J.; Wilk, L.; Nusair, M. *Can. J. Phys.* **1980**, *58*, 1200–1211.
- (62) Hamprecht, F. A.; Cohem, A. J.; Tozer, D. J.; Handy, N. C. *J. Chem. Phys.* **1998**, *109*, 6264.
- (63) Hammer, B.; Hansen, L. B.; Norskov, J. K. *Phys. Rev. B* **1999**, *59*, 7413.
- (64) Delley, B. *J. Chem. Phys.* **1990**, *92*, 508.
- (65) DMol³, release 4.0; Accelrys, Inc., CA, 2001.
- (66) Delley, B. *J. Chem. Phys.* **1990**, *92*, 508.
- (67) Weinert, M.; Davenport, J. W. *Phys. Rev. B* **1992**, *45*, 13709.
- (68) For example: Kruglik, S. G.; Ermolenkov, V. V.; Orlovich, V. A.; Turpin, P.-Y. *Chem. Phys.* **2003**, *286*, 97–108.
- (69) Pearson, R. G. *J. Am. Chem. Soc.* **1963**, *85*, 3533–3539.
- (70) Hemelsoet, K.; Lesthaeghe, D.; Van Speybroek, V.; Waroquier, M. *Chem. Phys. Lett.* **2006**, *419*, 10–15.
- (71) Klopman, G. The general perturbation theory of chemical reactivity and its applications. In *Chemical reactivity and reaction paths*; Klopman, G., Ed.; Wiley-Interscience: New York, 1974; pp 55–165.
- (72) Fukui, K.; Yonezawa, T.; Nagata, C. *Bull. Chem. Soc. Jpn.* **1954**, *27*, 423–427.
- (73) Fukui, K. *Science* **1987**, *218*, 747–754.
- (74) Parr, R. G.; Yang, W. *J. Am. Chem. Soc.* **1984**, *106*, 4049.
- (75) Kirner, J. F.; Garofalo, J., Jr.; Scheidt, W. R. *Inorg. Nucl. Chem. Lett.* **1975**, *11*, 107.
- (76) Sun, M.; Nelson, A. E.; Adjaye, J. *J. Mol. Catal. A* **2004**, *222*, 243–251.
- (77) Pettersen, R. C. *Acta Crystallogr. B* **1969**, *25*, 2527.
- (78) Lavoie, S.; Mahieu, G.; McBreen, P. H. *Angew. Chem., Int. Ed.* **2006**, *45*, 7404–7407.
- (79) Bencosme, C. S.; Romero, C.; Simoni, S. *Inorg. Chem.* **1985**, *24*, 1603–1604.
- (80) Higginbotham, E.; Hambright, P. *Inorg. Nucl. Chem. Lett.* **1972**, *8*, 747–750.
- (81) Su, Y. O.; Czernuszewicz, R. S.; Miller, L. A.; Spiro, T. G. *J. Am. Chem. Soc.* **1988**, *110*, 4150–4157.
- (82) For example: Dulak, M.; Bergougnant, R.; Fromm, K. M.; Hagemann, H. R.; Robin, A. Y.; Wesolowski, T. *Spectrochim. Acta A* **2006**, *64*, 532.
- (83) Kovalenko, A. Three-dimensional RISM theory for molecular liquids and solid-liquid interfaces. In *Understanding Chemical Reactivity: Molecular Theory of Solvation*, Hirata, F., Ed.; Kluwer Academic Publishers: Dordrecht, The Netherlands, 2003; Vol. 24, pp 169–275.
- (84) In the current literature, asphaltene structures are categorized as belonging to the continental or the archipelago models. The continental (or pericondensed) model is based on a core aromatic group containing a large number of fused rings (usually more than seven rings) with pendant aliphatic groups. The archipelago model suggests that asphaltenes consist of smaller aromatic groups (composed of 2–4 aromatic heterocyclic rings) linked by aliphatic bridges (Sheremata, J. M.; Gray, M. R.; Dettman, H. D.; McCaffrey, W. C. *Energy Fuels* **2004**, *18*, 1377 and references therein).

JP908641T